Temporal filtering and time-lapse inversion of geoelectrical data for long-term monitoring with application to a chlorinated hydrocarbon contaminated site

Nivorlis, Aristeidis; Rossi, Matteo; Dahlin, Torleif

Temporal filtering and time-lapse inversion of geoelectrical data for long-term monitoring with application to a chlorinated hydrocarbon contaminated site

Aristeidis Nivorlis [ID], Matteo Rossi and Torleif Dahlin

Engineering Geology, Lund University, Box 118, SE-22100 Lund, Sweden. E-mail: aristeidis.nivorlis@tg.lth.se

SUMMARY

We present a solution for long-term direct current resistivity and time-domain induced polarization (DCIP) monitoring, which consists of a monitoring system and the associated software that automates the data collection and processing. This paper describes the acquisition system that is used for remote data collection and then introduces the routines that have been developed for pre-processing of the monitoring data set. The collected data set is pre-processed using digital signal processing algorithms for outlier detection and removal; the resulting data set is then used for the inversion procedure. The suggested processing workflow is tested against a simulated time-lapse experiment and then applied to field data. The results from the simulation show that the suggested approach is very efficient for detecting changes in the subsurface; however, there are some limitations when no *a priori* information is used. Furthermore, the mean weekly data sets that are generated from the daily collected data can resolve low-frequency changes, making the approach a good option for monitoring experiments where slow changes occur (i.e. leachates in landfills, internal erosion in dams, bioremediation). The workflow is then used to process a large data set containing 20 months of daily monitoring data from a field site where a pilot test of *in situ* bioremediation is taking place. Based on the time-series analysis of the inverted data sets, we can detect two portions of the ground that show different geophysical properties and that coincide with the locations where the different fluids were injected. The approach that we used in this paper provides consistency in the data processing and has the possibility to be applied to further real-time geophysical monitoring in the future.

Key words: Electrical properties; Electrical resistivity tomography (ERT); Inverse theory; Numerical modelling; Time-series analysis.

INTRODUCTION

Contaminated ground has been recognized as a widespread problem in the past decades. There are cases of landfills affected by leakages with the potential to pollute the groundwater (Kelly 1966; Hopkins & Popalisky 1970; Apgar & Langmuir 1971; Cabral *et al.* 2000; Röling *et al.* 2000), and cases of excessive use of fertilizers and pesticides (Garrido *et al.* 2000; Kolpin *et al.* 2000; Liapis *et al.* 2000).

In Sweden, there are strict rules in place to avoid situations of industrial waste causing damage to the environment, but in the past, it was common that the waste was not handled properly and accidents with spills have been reported (Rai *et al.* 2019). This led to the contamination of many sites and in the national ongoing risk assessment more than 80 thousand sites have been identified as potentially contaminated (SEPA 2014). In that context, former dry-cleaning facilities and industrial sites are of particular interest.

Tetrachloroethylene (PCE) was mainly used as a cleaning product and in the latter as a degreaser, with little or no control of environmental impact until the 1980s. Several spills of the chemical occurred during the operation of these facilities that have led to chlorinated hydrocarbon (PCE) contamination of approximately 18 thousand sites in the country (SEPA 2014). Furthermore, industrial waste could also contaminate the soil and the underlying aquifers when not handled properly (Zhou *et al.* 2019; Vitali *et al.* 2021).

The expansion of cities creates a need for more space, and former industrial areas, once located in the suburbs of the cities, are strong candidates to provide expansion areas. There is a demand for efficient characterization and design of modern remediation plans to be applied in the aforementioned areas to reduce the risk of further spread of the problem and to make the ground suitable for expanding the current infrastructure network of the cities.

In this context, a collection of methods that are used for *in situ* remediation provides a modern cost-efficient and effective solution

that can be applied to reduce the concentration of the contaminant in the ground and prevent it from spreading any further. In case of *in situ* treatment contaminants are treated in place, typically by injected chemical substances (bioremediation) or by heating up the soil (thermal remediation) to speed up the degradation processes. In contrast with traditional methods (i.e. dig and treat), *in situ* remediation does not require the removal of the entire mass, which can lead to direct exposure to the contaminants and associated health concerns. Furthermore, in cases where the contaminant mass has large volume or is deeply buried, *in situ* remediation may be the only option, or it is preferable because it can drastically reduce the overall cost of the remediation. The development of tools for efficient characterization and monitoring of the on-going *in situ* remediation is an essential aspect of the process (Ottosen *et al*. 2021).

Analysis of groundwater and soil samples, while the remediation is on-going, provides necessary quantification and can be used to monitor changes in the subsurface accurately (Sedlazeck *et al*. 2020). The information provided is however localized at a point and often quite limited due to the cost related to the collection and analysis of the samples. Furthermore, it requires qualified staff to interact directly with the contaminant, which can dramatically increase the budget and therefore should be kept to the minimum. Geophysical monitoring can provide a valuable tool to interpolate the sparse and point information from the groundwater and soil samples and monitor more effectively the changes in the subsurface, both in space and time (Mishra *et al*. 2019). Geophysical methods can also be used as a base for designing a drilling and sampling program that is as representative as possible, or to identify spots where an existing sampling program needs to be augmented (Danielsen & Dahlin 2009, 2012; Ronczka *et al*. 2018).

The direct current (DC) resistivity method has been successfully used in a broad spectrum of subsurface investigations (Loke *et al*. 2013) such as environmental (Forquet & French 2012; Auken *et al*. 2014; Fernandez *et al*. 2019), engineering geology (Danielsen & Dahlin 2009; Rossi *et al*. 2018; Abdulsamad *et al*. 2019) and hydrogeological (Fetter 2001; Leroux & Dahlin 2006; Chirindja *et al*. 2017; Zago *et al*. 2020). The DC resistivity method was successfully applied for landfill characterization (Bernstone *et al*. 2000; Chambers *et al*. 2006), where the induced polarization (IP) method, an extension of the traditional DC resistivity method, has also been used (Gazoty *et al*. 2012; Ustra *et al*. 2012; Ntarlagiannis *et al*. 2016; Power *et al*. 2018). Microbial activity can produce electrical signals (Atekwana *et al*. 2005) that can be detected with geophysics (Davis & Atekwana 2006; Davis *et al*. 2006; Atekwana & Atekwana 2010; Heenan *et al*. 2015).

Contaminated sites have been investigated using frequency-domain IP (Cassiani *et al*. 2009; Flores Orozco *et al*. 2012a) and time-domain IP (Ntarlagiannis *et al*. 2016; Johansson *et al*. 2017; Sparrenbom *et al*. 2017; Maurya *et al*. 2018b). Frequency-domain IP has been used for monitoring of uranium bioremediation (Flores Orozco *et al*. 2013) and the injection of zerovalent iron particles (Flores Orozco *et al*. 2015). The direct current resistivity and induced polarization (DCIP) method can be used in a time-lapse framework (Power *et al*. 2014; Kuras *et al*. 2016) and has been successfully applied for monitoring contamination (Park *et al*. 2016; Caterina *et al*. 2017; Sparrenbom *et al*. 2017).

Recent advances in the DCIP method have reduced drastically the data acquisition time (Olsson *et al*. 2015) and advanced signal processing algorithms can provide higher quality data by increasing the signal to noise ratio (Olsson *et al*. 2016). Traditional autonomous monitoring systems (Chambers *et al*. 2009) that can provide frequent reliable data (i.e. daily) to monitor the changes in

the subsurface do not generally adapt those recent developments and focus mainly on resistivity measurements (Chambers *et al*. 2009; Sjödahl *et al*. 2009). For frequency-domain IP measurements reciprocals are often used to quantify the measurement error (Flores Orozco *et al*. 2012b) and this idea has been applied to monitoring data (Flores Orozco *et al*. 2019). Reciprocal error analysis can also be used in time-domain measurements (Saneiyan *et al*. 2019); however, it is often restrictive as the use of dipole–dipole arrays is required. Nested arrays can be well optimized for modern multichannel instruments, they have higher signal to noise ratio but they make the use of reciprocals practically impossible, as the time required can be increase by a factor of 4. There is a need for similar tools that can be applied to DCIP monitoring data to remove temporal outliers and provide better representations of the changes in the subsurface, so that they can then be further linked with the underlying changes in the ground (Heenan *et al*. 2015; Saneiyan *et al*. 2019).

In this study, we propose a complete workflow for DCIP data collection, pre-processing and inversion, which uses digital signal processing algorithms for automated outline removal. The proposed workflow is tested against a synthetic geoelectrical time-lapse experiment and then applied to field data. The field data were collected in an active test site where a pilot remediation experiment is on-going in a former dry-cleaning facility in Sweden, contaminated with chlorinated solvents (PCE). The remediation started in November 2017 and the collected data until July 2019 will here be analysed and presented.

METHOD DESCRIPTION

Direct current resistivity and time-domain induced polarization

The DC resistivity method is performed by injecting direct current in the ground from two electrodes (A and B) and measuring the difference in potential between another pair of electrodes (M and N). The injected current creates a potential field that is governed by the electrical properties of the subsurface and it is described through a Poisson's equation (Loke *et al*. 2013). The overall aim of a DC resistivity survey is to reconstruct the subsurface electrical properties. It is achieved by measuring many combinations of current and potential electrode pairs, typically along a line for a 2-D case, to be able to describe the electrical field in order to infer the distribution of the electrical conductivity in the ground. The electrical resistivity can then be computed as it is simply the inverse of the electrical conductivity and can be related, among other things, to different lithologies, porosity, moisture content, fluid chemistry and contaminants (Brunet *et al*. 2010; Mainoo *et al*. 2019; Mgbolu *et al*. 2019; Wang *et al*. 2020; Gamal *et al*. 2021).

The time-domain IP method measures the ability of the ground to store electric energy while the current is injected (on-time) which is then released, in form of current, when the current is turned off (off-time). The parameter that describes how much energy is stored in the ground is called chargeability, and it can also be measured in the on-time using a 100 per cent duty cycle (Olsson *et al*. 2015). The chargeability is a physical parameter that can be affected by mineralization, heavy metals, contamination (Telford *et al*. 1991) and can be linked with hydraulic permeability (Maurya *et al*. 2018a; Weller & Slater 2019).

Automation

In a long-term monitoring experiment, it is imperative to fully automate the workflow of acquiring, processing and inverting the data sets, as it quickly becomes impossible to manually process the entire monitoring data set. For this reason, there is a need for a complete workflow with routines for automated data collection and handling (quality control and transferring). Then advanced signal processing algorithms are needed for automated outline detection and noise removal from the collected data sets. The filtered data should then be prepared for the inversion using efficient routines suitable for long time-series of monitoring data and finally to be visualized for further interpretation.

Long-term monitoring system

First and foremost, an autonomous and automated data acquisition system is needed to provide resistivity and chargeability data. Secondly, the data handling component is responsible for transferring the data from the remote location, the contaminated site, to the available resources for further processing and archiving of data.

For the data acquisition, we use an ABEM Terrameter LS2, which is paired with external relay switches to extend its capabilities and allow more electrode spreads to be connected with the instrument. The relay switches include an ABEM Electrode Selector ES10-64C, plus four two-way switch units with integrated transient protection for each individual electrode (designed and built at Lund University). The measurements are performed using the 100 per cent duty-cycle IP mode option (Olsson *et al.* 2015) where both resistivity and chargeability are measured during the on-time, which effectively reduces the amount of time by close to half and increases the signal to noise ratio. This measurement method is based on the processing of full-waveform data developed by Olsson *et al.* (2016).

Software that communicates (via secure shell connection) with the instrument and the relay switches was developed, ensuring that the system can measure multiple profiles (spreads) sequentially on a daily basis or as specified by the user. The software long term monitoring system (LoTeMoSy) is written in Python and runs on a compact PC (industrial grade to ensure longevity), which sits next to the geophysical instrument and controls the entire monitoring sequence autonomously without the need of human interaction. Once the measurement sequence is complete, the data are transferred from the field PC to a server for further processing and archiving.

Digital signal processing

Geophysical data are generally contaminated by noise that needs to be identified and removed before the data are further processed and interpreted. The source of noise could be external power sources, natural currents or hardware problems, and it is important to identify and remove noisy measurements that could potentially corrupt the results. The changes in the subsurface due to seasonal variation or the effects from the remediation are expected to be smooth, apart from the injection of degradation products, whereas rainfall or frozen ground could introduce sharper changes in the daily measurements.

The apparent resistivity pseudo-sections, like the ones presented in Fig. 1, are generally a useful tool for qualitative inspection of the spatial distribution of the data, as values should not be much different from their neighbouring values. It is evident that there are time steps (Fig. 1, left-hand column), where some data points are affected by dominant noise, showing extreme differences from their neighbouring values.

The temporal distribution is a key factor that can be used when working with high-frequency sampling data as it is possible to analyse each individual measurement over a period. If the noise is incoherent, the spatial inconsistency that can appear in a single profile will normally affect a limited number of measurements for few time steps; therefore, it will not remain dominant for longer periods. The source of noise can be external, such as electromagnetic induction from buried facilities; or internal from the system, as for example coupling in electrode cables. It is also evident that often the instrument cannot inject enough current (Fig. 2), either due to high contact resistance, which is often caused by frozen ground during the winter period and could cause severe data quality issues, or some random hardware failure.

As shown in Fig. 1 (left-hand column), there are several data points that show extremely low apparent resistivities for 4 days (here exemplified by data collected on a monitoring site from 16th and 18th of November), before the measurements became stable. The analysis of the time-series of each individual data point (quadrupole) can be used to identify and eliminate points that show anomalous high-frequency fluctuations over time.

Fig. 2 illustrates an example of a time-series of a single quadrupole that can used to identify abrupt changes in the geophysical parameters. Extremely low values, which can also be identified in the pseudo-sections of Fig. 1, are present in single time steps and they cannot be explained by natural processes that occur at lower frequencies. Some sharp transitions are more consistent (March 2018 and February 2019) and they are related to seasonal variations, specifically to frozen ground as others appear only for a short time and they could be related to sudden changes, due to a rainfall event, or simple erratic measurements. There is a need to develop a software imposed digital filter, that is applied to the entire data set on individual time-series of quadrupoles (Fig. 2) and that removes outliers that are related to erratic measurements. Preserve changes appear to be consistent in the data set, while dampening sharper sporadic changes appear to be unrelated with the processes that are to be investigated.

The signal processing algorithm consists of two steps. First, a moving window median filter is applied with the aim of removing extreme outliers. The filter is applied with a window length of 7 days (weekly). The second step is a low-pass Butterworth (LPB) filter to further smooth the temporal series removing the higher frequency changes that may be related to noisy data points while preserving the information from the low-frequency changes, which are of most interesting for geophysical monitoring applications, as the processes of interest take time to develop (Sjödahl *et al.* 2009; Heenan *et al.* 2015; Caterina *et al.* 2017). The filter has a normalized threshold frequency fixed at 12 per cent of the Nyquist frequency and order 2; the frequency response of the filter is presented in Fig. 3. The filters are included in the SciPy (scientific python) open-source library (Virtanen *et al.* 2020), which is available for the Python programming language.

Fig. 4 represents an example of the filter applied to a single quadrupole; the blue line shows the original data and the green line shows the filtered data. The same filter (median and LPB) was applied to every quadruple to eliminate the outliers and replace them with a filtered value that matches past and future values, in order to avoid having missing data as an input to the inversion. The relative fluctuation in chargeability values appears stronger because the signal to noise ratio is lower. The chargeability values are generally in a narrow range of few mV/V (from 1 to 10) for
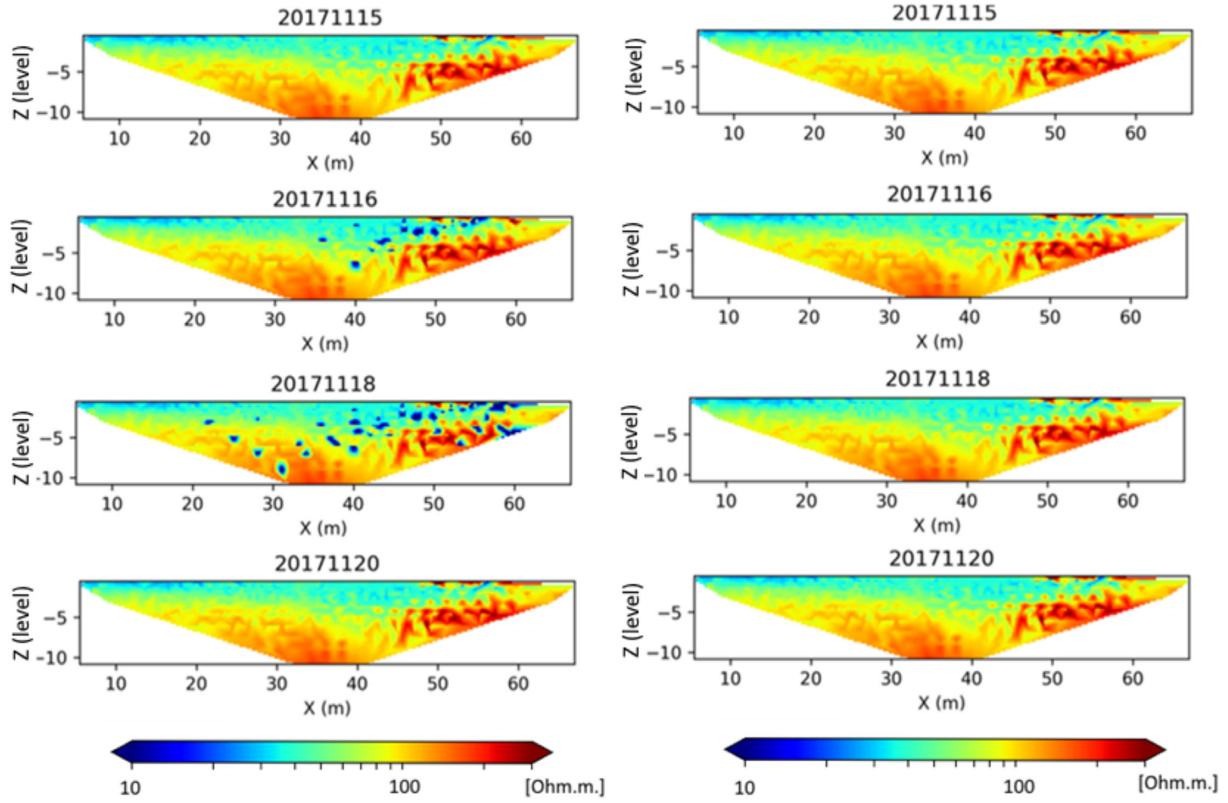
Figure 1. Examples of pseudo-sections for selected days: in the left-hand column, pseudo-sections of raw data; in the right-hand column, the pseudo-sections of the processed data sets. Dates are in YYYYMMDD format. We can identify spatial outliers that appear in the dates 2017 November 16–19 and that are removed by the processing framework.
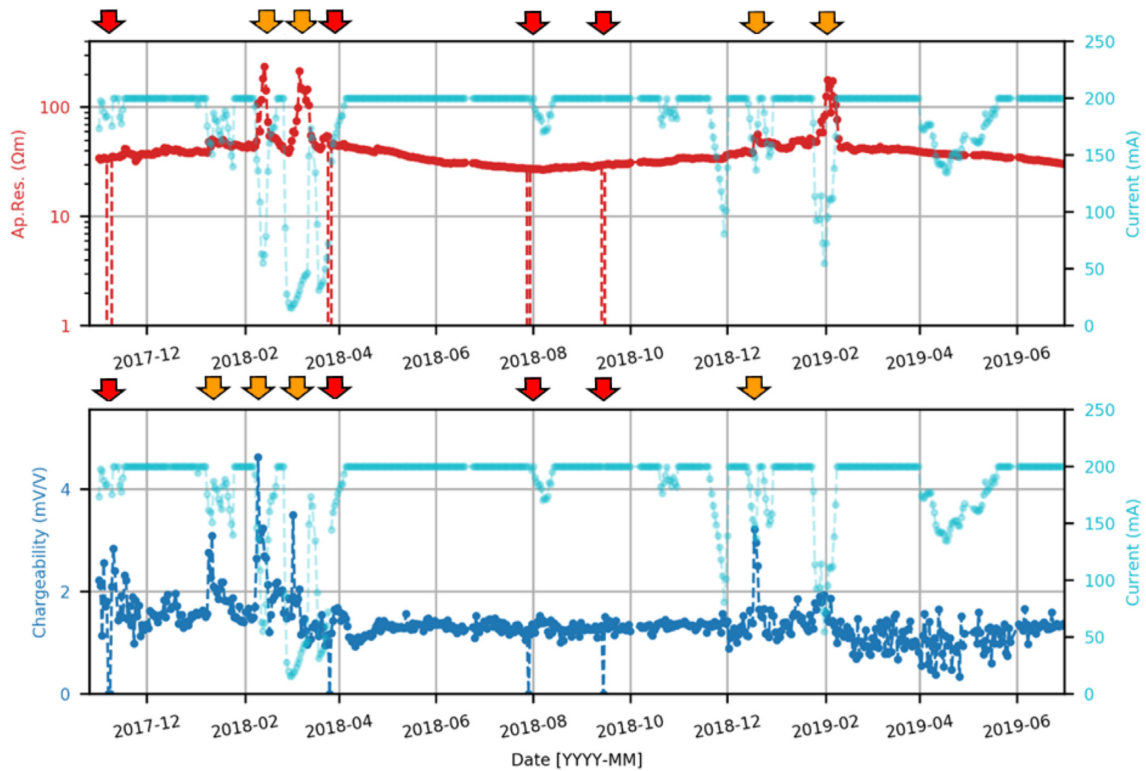

Figure 2. Example of the time-series of raw data for a single quadrupole. The cyan lines indicate the current injection, the red line indicates the apparent resistivity and the blue line indicates the apparent chargeability as measured by the instrument. The example refers to the data point involving electrodes' distance 44-53-49-50 m (A-B-M-N) of Line 3. The arrows indicate examples of bad/missing data (red) and outliers related to low signal levels (orange).
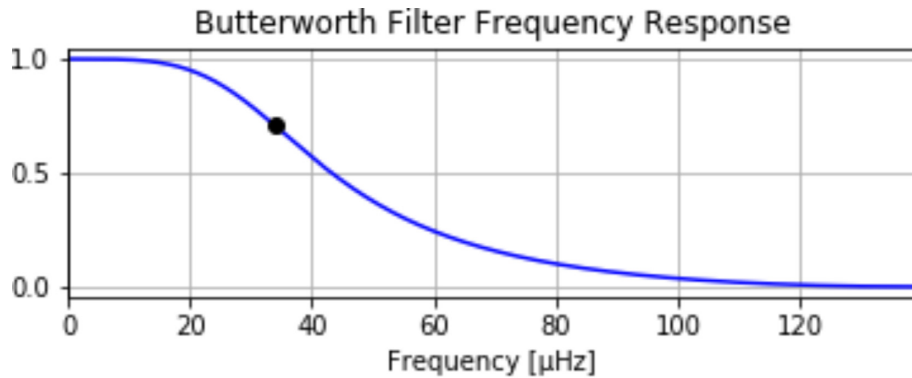
Figure 3. The frequency response of the low pass Butterworth filter. The frequency of the measurements was set at 1/3600 Hz and the frequency cut-off was set to 34 μHz.
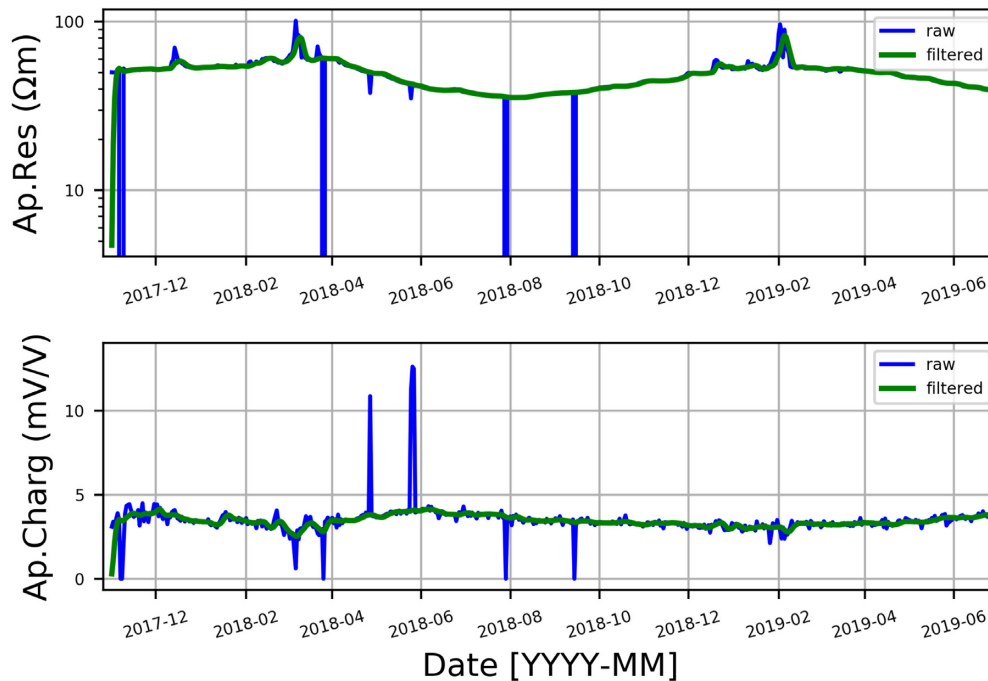

Figure 4. Example of filtering of raw data for quadrupole 34 of Line 3. The example refers to the data point involving electrodes distance 7-16-13-14 m (A-B-M-N).

the entire data set, as it can be seen in the time-series of individual quadrupoles.

Extremely sharp and inconsistent changes in the apparent resistivities cannot be explained by natural events, neither sudden (i.e. rainfall) nor slower (i.e. seasonal variations due to temperature effects). Furthermore, the aim of the proposed methodology is to be applied in investigations where slowly occurring processes, such as *in situ* remediation, leakage in landfills or internal erosion in dams, are to be investigated. The changes due to such processes are expected to be smooth, less dominant in amplitude and consistent in time, therefore it is evident that sharp changes are not relevant in that context and should be identified and removed from the data.

Inversion

The inversion software Geotomo Res2DInv (v4.09) has been used in this work with an L1-norm smoothness constrain, both in space and time.

Inversion of large data sets can be computationally challenging, and therefore efficient routines for handling monitoring data need to be addressed. In this work, it was decided to invert weekly average data sets, to have an overview of the main changes that affect the geophysical parameters, adding further smoothing steps, as the principal interest is to investigate the long-term. Weekly averages provide a good compromise to reduce the computation cost required to invert daily data while preserving the expected changes, as it is shown in the simulated experiment which is presented later. The weekly results aim to provide an overall understanding of how the subsurface is changing, while keeping the computational cost to the minimum.

SIMULATION OF A MONITORING EXPERIMENT

The proposed workflow for efficient processing and inversion of time-lapse data sets was first tested against a synthetic geoelectrical

data set that simulates a yearly time-lapse experiment. For this purpose, a baseline geoelectrical model was constructed (Fig. 5, top) and the geoelectrical properties of each unit were altered to generate 365 forward models where each model represent every single day of the experiment. The simulated models were generated using pyBERT, which is based on the open source software pyGIMLi (Rücker *et al.* 2017).

Model space

The base geoelectrical model consists of two layers with the addition of two areas where the changes are simulated. Fig. 5 shows the geoelectrical model that consists of clay (yellow), crystalline bedrock (red), block A (green) and block B (blue). The model resistivities are 30 Ω m for the clay layer, 3000 Ω m for the crystalline bedrock, 30 Ω m for block A and 200 Ω m for block B. Then, the resistivities of each unit were altered for each consecutive day to simulate seasonal changes in the entire clay layer (Fig. 5, bottom left), a small increase in resistivity for block A (Fig. 5, centre) and a rapid decrease in resistivity for block B (Fig. 5, right).

Finally, once the 365 different resistivity distributions within the same geometrical framework were constructed (one for each day), we used pyBERT to calculate the forward response for each individual model using a multiple gradient array with identical geometry and measurement sequence as the one used in the field example that follows. The array consists of 1384 measurements in total with 1 meter separation between the electrodes.

The resulting synthetic data set is contaminated with noise to simulate a more realistic scenario. A two-steps approach is applied by first adding 2 per cent white noise and then including random spikes with likelihood of 5 per cent. The processing was performed on every single quadrupole of the time-series.

An example of an individual quadrupole is shown in Fig. 6. The blue line represents the contaminated signal (for an entire year) and the green line represents the filtered signal using the proposed methodology. The filtered signal (green line) successfully removes the spikes and smooths the random noise. The proposed filtering methodology is applied to each quadrupole of the synthetic data set. Weekly average data sets, as it was described in the previous section, are extracted and inverted against a common baseline model, which in the case is the initial geoelectrical model (Fig. 5, top).

Fig. 7 illustrates the inverted baseline model (top) and the results of the time-lapse inversion for the entire experiment. The resistivity of block A (Fig. 7 bottom left, green line) is resolved accurately with a small deviation from the starting model. Furthermore, the resistivity changes compared to the baseline (Fig. 7 bottom right, green line) show that the general trend is resolved relatively well, especially for the first 6 months. The resistivity value for block B (Fig. 7 bottom left, blue line) is not resolved as well as for block A, which can be attributed to an inherent issue of the inversion as it is generally smoothing the results. However, even in this extreme case it is possible to follow the general trend relatively well (Fig. 7 bottom right, blue line). The result is promising as in time-lapse experiments it is mainly the variation of the electrical properties during time that is used in the interpretations. If the actual values are of interest, then an inversion scheme with sharp boundaries and the use of *a priori* information (Fortier *et al.* 2008) needs to be used instead; however, this is beyond the scope of the work presented in this paper.

Lastly, it is extremely important to take into consideration the seasonal changes that have been included in the clay layer (Fig. 5,

bottom left). Such seasonal changes are usually present in the time-lapse monitoring and if their magnitude is larger than local changes in the area of interest (for example that is the case for block A), they might mask weak signal due to different processes.

The suggested methodology can be efficient to handle noisy data that can potentially contain also missing values, without excluding entire quadrupoles from the final data set. The analysis of the synthetic experiment shows that the suggested methodology appears to be applicable to large monitoring data sets. However, as it was discussed previously, in cases where the seasonal variations are dominant or changes of lower amplitudes are to be investigated a more detailed analysis should be used. Even so, the proposed methodology can be used to highlight periods of interest in a large data set, e.g. few years of high-frequency monitoring, which otherwise would have been extremely time-consuming to investigate.

FIELD DATA

Site description

The area of investigation is an industrial-scale dry-cleaning facility (Alingsåstvätteriet) located in Alingsås, Sweden. Around the 1960s or 1970s, a single documented spill of approximately 200L PCE leaked into the ground; however, other undocumented incidents might have occurred. The spread of PCE led to the formation of a DNAPL source zone underneath the building. Over the years, the contaminant has migrated as a result of the groundwater flow and the bedrock topography (Nivorlis *et al.* 2019), forming a larger DNAPL plume.

The contaminants are mostly present in the fine-grained quaternary deposit (silty clay), which is dominant in the subsurface and extends from 2 to 7 m depth. The current geological model (Nivorlis *et al.* 2019) suggests that a small amount is leaking through the thinner and coarser layer underneath and spreading downgradient. Based on soundings and well logs the crystalline bedrock can be found at 7–9 m depth, and based on previous investigations (Nivorlis *et al.* 2019) it is believed to be intact and act as an impermeable layer in our conceptual model. The geological conceptual model is based on the membrane interface probe (MIP) soundings investigation and indicates that the highest concentrations of the contaminants are found in the clay layer. A pilot *in situ* remediation plan was designed using a direct push injection method. Two different commercial fluids, a mixture of bacteria (SDC-9™) with a carbon source (Provectus ERD-CH4) and iron particles (Trap & Treat® Bacteria concentrate), were injected in two different areas adjacent to each other, to evaluate their effectiveness for future use (Nivorlis *et al.* 2019). Fig. 8 presents the locations of the direct push injections for Area A (purple) where the mixture of bacteria with the carbon source (Provectus ERD-CH4) was injected and Area B (orange) where iron particles (CAT100) were injected.

Monitoring system

In the Alingsås site, we have installed the monitoring system described previously and four DCIP profiles are measured daily. Each profile has 64 stainless steel electrodes with 1 m electrode spacing except at the end of the layouts where the electrode spacing is 2 m (see Fig. 9). Stainless steel electrodes are well suited for measuring resistivity as well as time-domain IP, the latter provided that an instrument with sufficient dynamic resolution and proper signal handling is used (Dahlin *et al.* 2002). Furthermore stainless steel
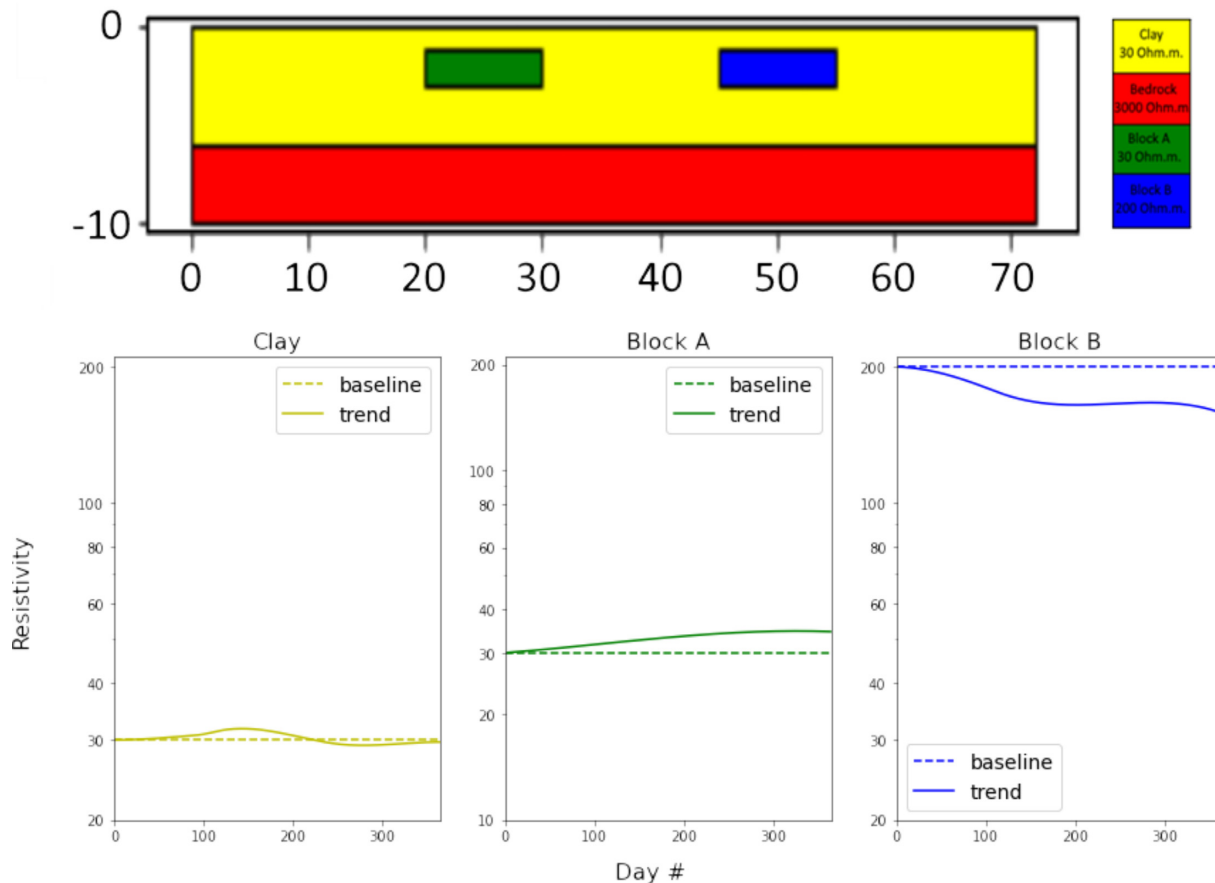
Figure 5. Geoelectrical units of the baseline model (top) consisting of clay (yellow), crystalline bedrock (red), block A (green) and block B (blue). The introduced resistivity variation is presented for the clay (bottom left), block A (bottom centre) and block B (bottom right).
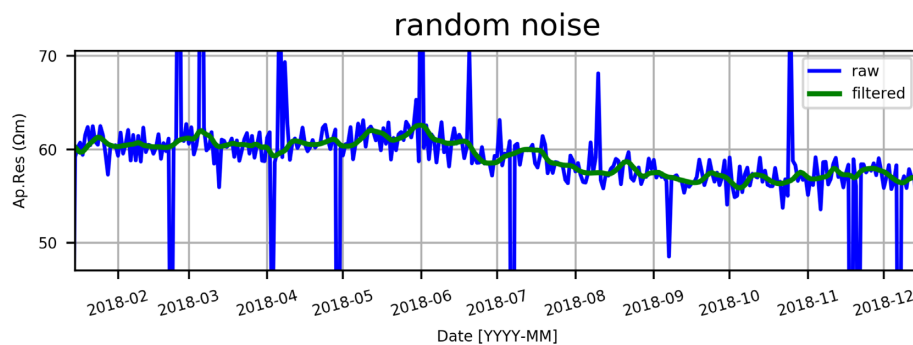

Figure 6. Signal processing filtering of individual quadrupole. The blue lines indicate the original signal (contaminated with random noise and spikes) and the green line indicates the filtering result.

electrodes are robust and long-term stable for monitoring installations (Sjödahl *et al.* 2008; Kuras *et al.* 2016; Arosio *et al.* 2017). The horizontally placed plate electrodes (10 cm × 10 cm) and the cables are buried into the ground at approximately 30 cm depth to minimize interference and provide a permanent installation of the system (Nivorlis *et al.* 2019). The installation resulted in relatively good electrode to ground contact with mean electrode resistances of around 1 kΩ in the initial test measurements (Figs 9a and b). The contact resistances have remained stable throughout the monitoring period except for peaks in cold periods with ground freezing during winter (Fig. 9c). The relatively low contact resistances during most of the year suggest that good quality IP data may be acquired, even if

the same single multi-core electrode cables are used both for current transmission and potential measurements (Dahlin & Leroux 2012).

The measurements are taken using the multiple gradient array (Dahlin & Zhou 2006) with a total of 1384 measurement. A multiple gradient array is generally described using the *s*-factor, which is the relative length of the current dipole, counted as multiples of the potential electrode spacing *a*. The *s*-factor is 9 in the majority of the measurements and only few data points have larger *s* values in connection with larger electrode separations at the layout extremities. The *a* parameter has values from 1 to 7, except at the end of the spreads where *a*-values are up to 14. The current pulses are 4 s long in order to enable high-quality IP data (Maurya *et al.*
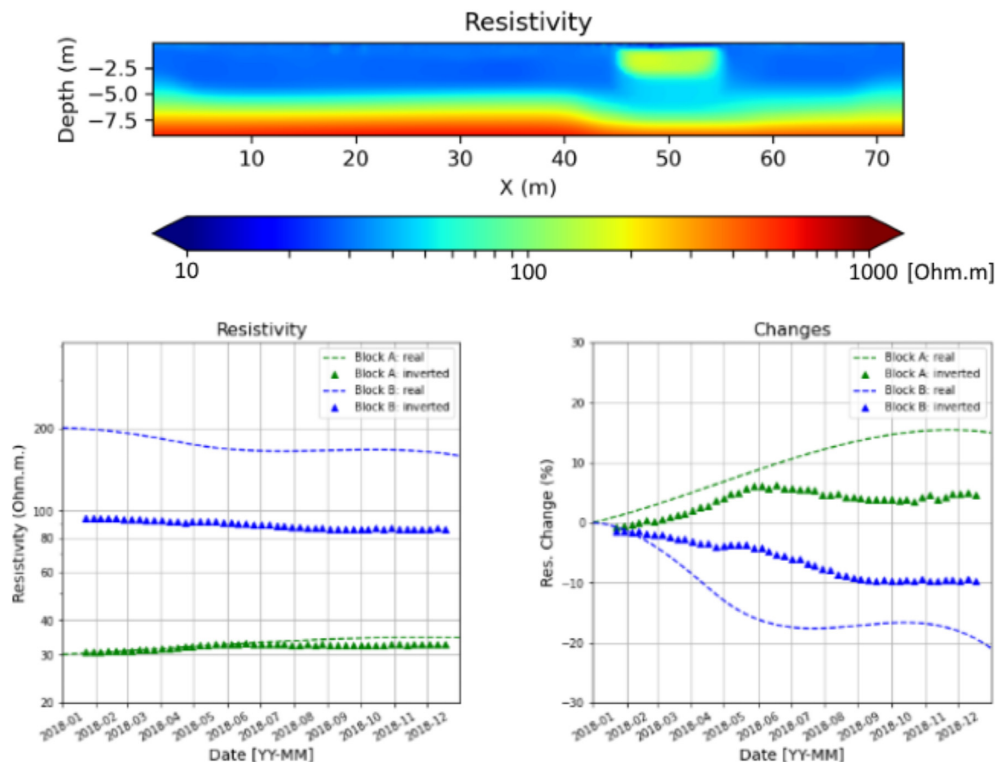
Figure 7. The inverted result of the baseline model is presented in the top figure. The time-lapse inversion results are presented in the bottom figure with green for block A and blue for block B. The left-hand figure shows the average resistivity for each block.
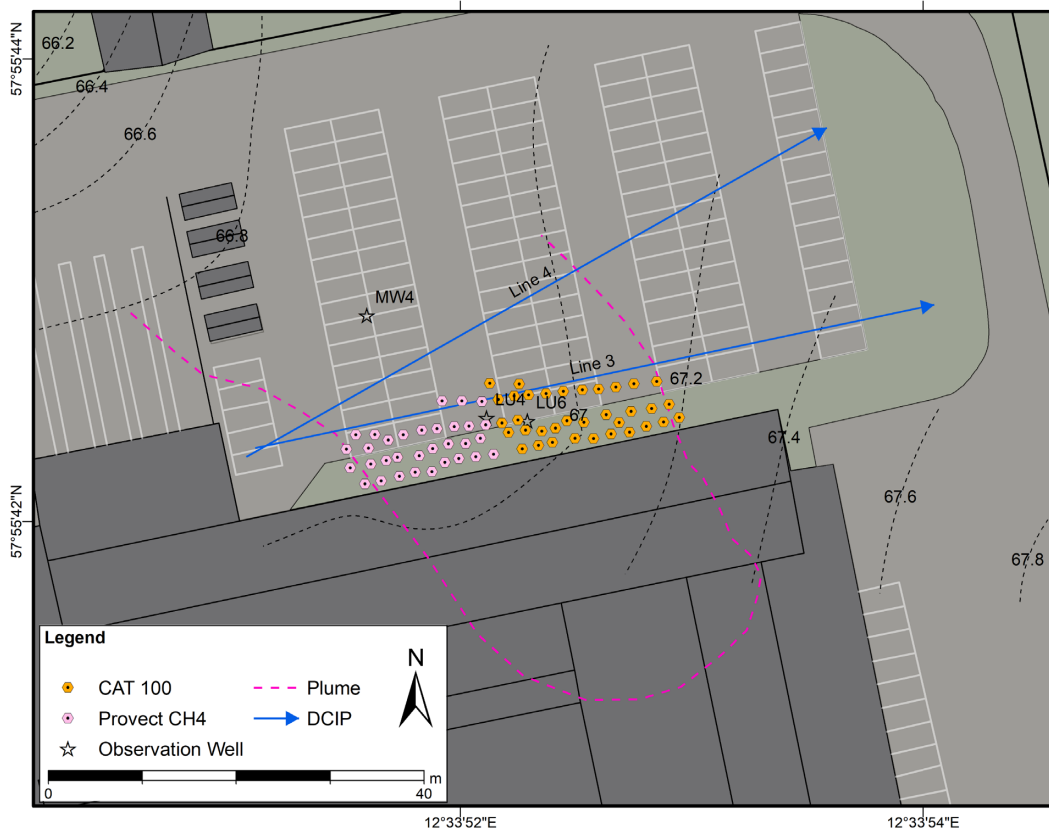

Figure 8. Alingsås field site. DCIP monitoring lines (solid blue) with the arrow that indicates the direction of local coordinates, interpreted DNAPL plume boundaries (pink dashed line), the observation wells used to collect the water samples (black asterisk) and the injection points of CAT100 (orange) and Provect CH4 (purple). The dashed black lines indicate the groundwater level measured in September 2017.
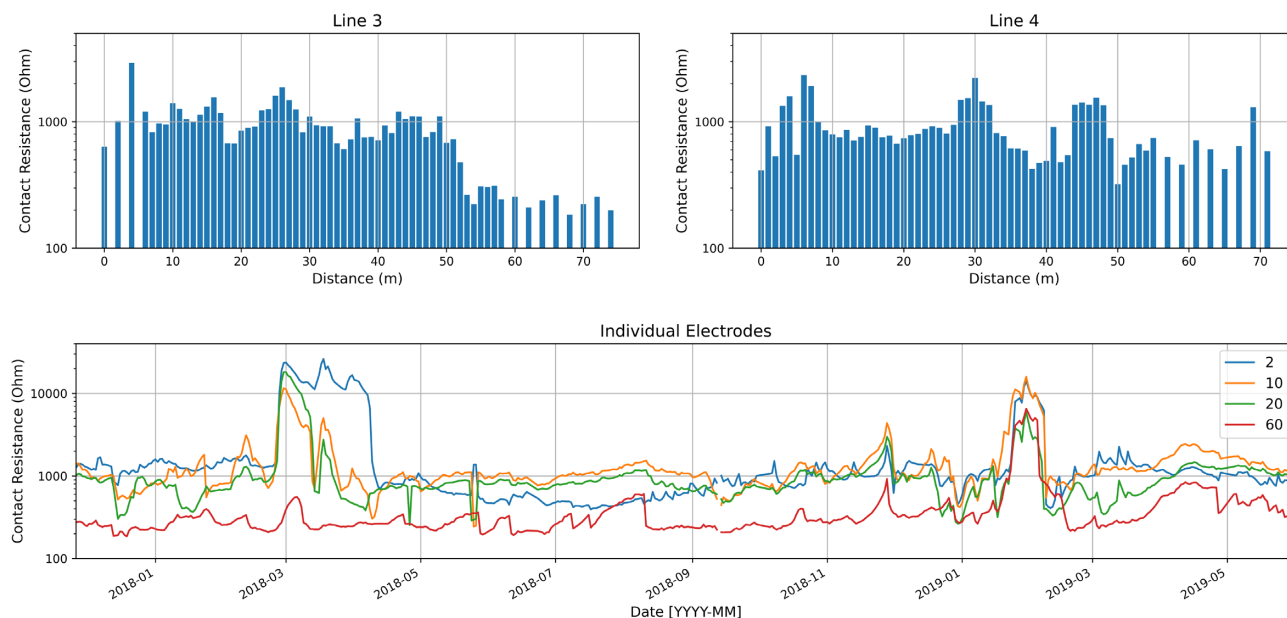
Figure 9. Example electrodes contact resistances for Line 3 (top left), Line 4 (top right) and temporal variation for selected electrodes from Line 4 (bottom).

2018b; Olsson *et al.* 2019), and four pulses are used for stacking to increase the signal to noise ratio of each measurement and quantify repeatability.

Unfortunately, the monitoring system installation was finished only 10 days before the remediation plan was scheduled to start, as we could not have access to the site and the equipment earlier. Ideally, a longer series of data should have been acquired before changes start to happen in the subsurface due to remediation, but it was neither possible to postpone the remediation plan nor to access the site earlier due to logistical issues. The monitoring system is running continuously until today and in this work, we have analysed and present the data that cover a period of 20 months, from November 2017 to June 2019.

Baseline results

A key aspect of inverting time-lapse data is the identification of a reference model (or baseline). The first 11 days of acquisition, before any remediation action took place, were inspected to assess a stable baseline data set (Fig. 10). After excluding two missing (uncollected) time steps (7th and 8th of November 2017), the remaining values of the time-series are averaged for each single quadrupole to establish a robust baseline reference model.

The data collected in the field where first processed by the scheme proposed in this work to remove spatial and temporal outliers. Then, weekly averages were extracted (Fig. 11) for every week following the end of the baseline, which was inverted against the average reference model using the time-lapse constrained mentioned previously. Even if it is possible to fine-tune each individual inversion, the scope of this work is to build a robust framework that can be applied with the same settings for long-term monitoring projects. In many cases, data can be collected for years, therefore individual fine-tuning of daily, weekly or monthly data is practically impossible. The resistivity distribution along Line 4 (Fig. 12) clearly identifies the crystalline bedrock as a high resistivity bottom layer at around 7 m from topographic surface. A shallow high resistivity filling material, apparently thinner than 1 m, can also be identified. The resistivities of the underlying natural sediments range from 10

to 40 Ω m. An area with an increased resistivity response is present between approximately 0 and 35 m along the profile at a depth of 2.5–5 m. This anomaly correlates with higher concentrations of the contaminants as pointed out by Nivorlis *et al.* (2019; see also the position of plume boundaries in Fig. 8). The chargeability response should not be affected by any infrastructure along Line 4 and there is a generally flat response with very low chargeability values (less than 4 mV V^{-1}).

The resistivity distribution of Line3 (Fig. 13) shows a shallower high resistivity bedrock at around 5–6 m from topographic surface. The transition between quaternary sediments and crystalline metamorphic bedrock is shallower than in Line 4, since the bedrock topography is dipping towards north (Nivorlis *et al.* 2019). The top filling material, with a maximum thickness of about 1 m, stands out with higher resistivity than the glaciofluvial sediments below. The sediments are defined by resistivity values between 20 and 40 Ω m. Along this profile, a higher concentration of contaminants (Nivorlis *et al.* 2019) correlates with an increase in resistivity between 0 and 30 m along the profile (Eastern part). The chargeability values are rather homogeneous in the subsurface with moderate values (<10 mV V^{-1}), except for a high chargeability response at around 22 m of the profile, which is correlated with buried infrastructures.

Time-lapse results

The time-lapse results of weekly average data inverted against the baseline are shown in Fig. 14 for Line 4 and Fig. 15 for Line 3. Only three selected time-steps of the entire time-series are displayed and are presented as percentage variation of resistivity and absolute change in chargeability (chargeability values are close to zero, so percentage variation should be avoided they grow to infinity as chargeability goes to zero) compared to the averaged baseline.

Analysing the time-lapse results for Line 4 (Fig. 14), mostly seasonal variations are observed, since the line is located several meters away from the area where the pilot remediation test is conducted (see Fig. 8). The severe effect of frozen ground in the data sets around 2018 March 8 and 2019 February 27 appears as a strong increase in resistivity in the shallower depths, 2 and 0.5 m, respectively. The
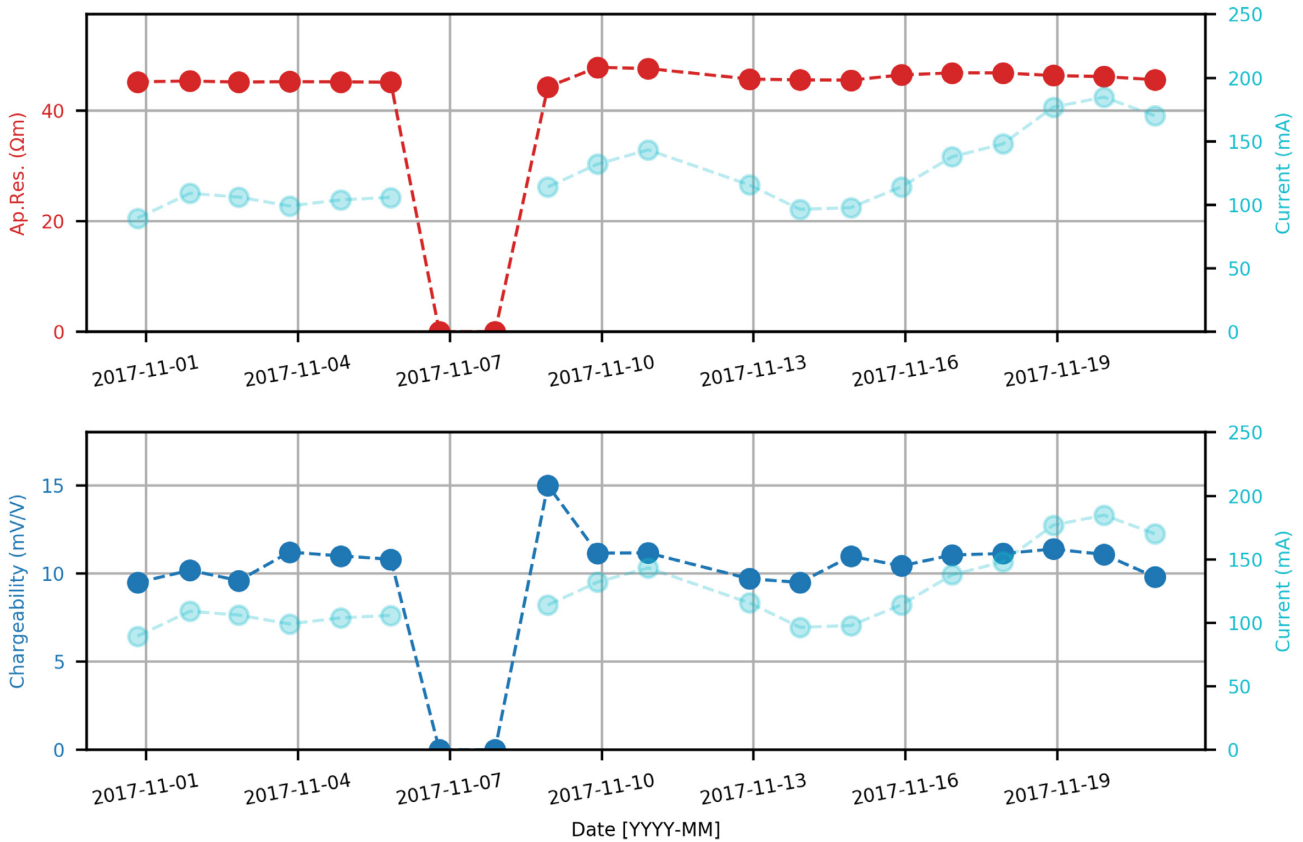
Figure 10. Example of electrical resistivity and integral chargeability time-series data of a single quadrupole acquired before the remediation took place (started on 8th of November). The example refers to the data point involving electrodes distance 26-35-29-30 m (A-B-M-N) of Line 3.
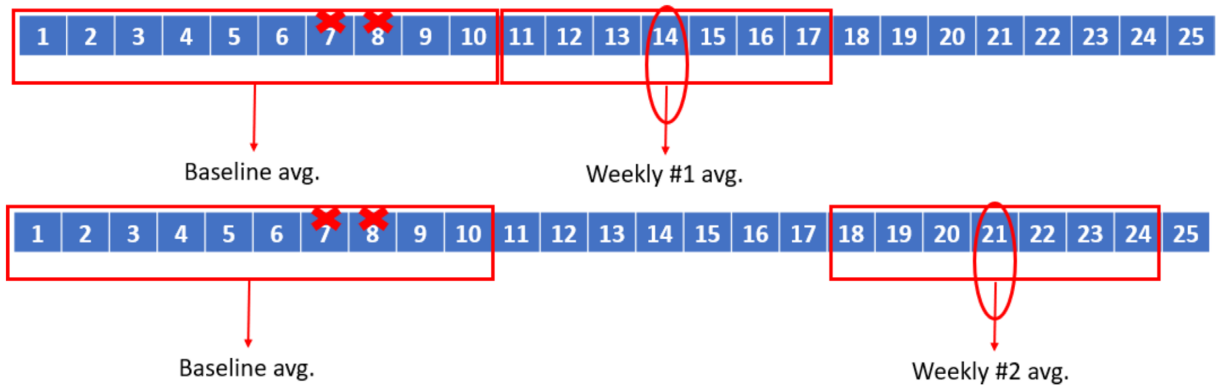

Figure 11. Time-lapse inversion of weekly averages against a constant average reference. The cells represent daily acquisitions. The 7th and 8th day were not included in the reference data set (see Fig. 10)

upper soil was fully saturated (after a period of intense precipitation) during the installation of the monitoring system, which must have affected the baseline reference data set. Further changes can be identified in the 3 m depth of time-step 2018 October 21 that may probably relate to variations in the elevation of the groundwater table. The chargeability variations appear rather stable over the monitoring period, with small variations within in the range of ± 2 mV V^{-1}.

The time-lapse results for Line 3 (Fig. 15) are expected to be more complex due to the proximity of the remediation experiment and the infrastructures connected to the building. For this reason, the results from Line 4 (Fig. 14) can be used to identify similar seasonal effects along Line 3. Analogous seasonal variations can

be identified due to the frozen ground in the winter periods (dates 2018 March 8 and 2019 February 27).

When the frozen ground retreats, different responses are observed, both in Line 3 and Line 4, coming from the areas where the remediation products were injected. In Fig. 15, a general decrease is identified in the resistivity in the central area of Line 3 (from 20 to 40 m along the profile) that is consistent for the entire analysed period and coincides with the portion of soil treated with zerovalent iron particles. In the western area (from 7 to 24 m along the profile), where the bacteria consortium was injected, the response shows a similar behaviour as the untreated part in the far right (eastern) side with a rather seasonal pattern. The chargeability is greatly affected by the high response of some probable buried infrastructure
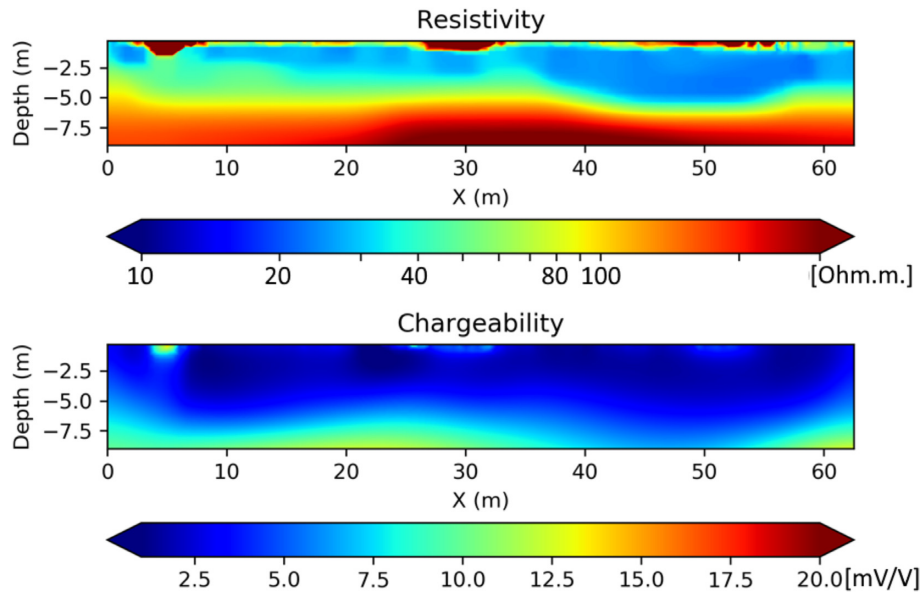
Figure 12. Inverted model for resistivity (top) and chargeability (bottom) of the baseline for Line 4.
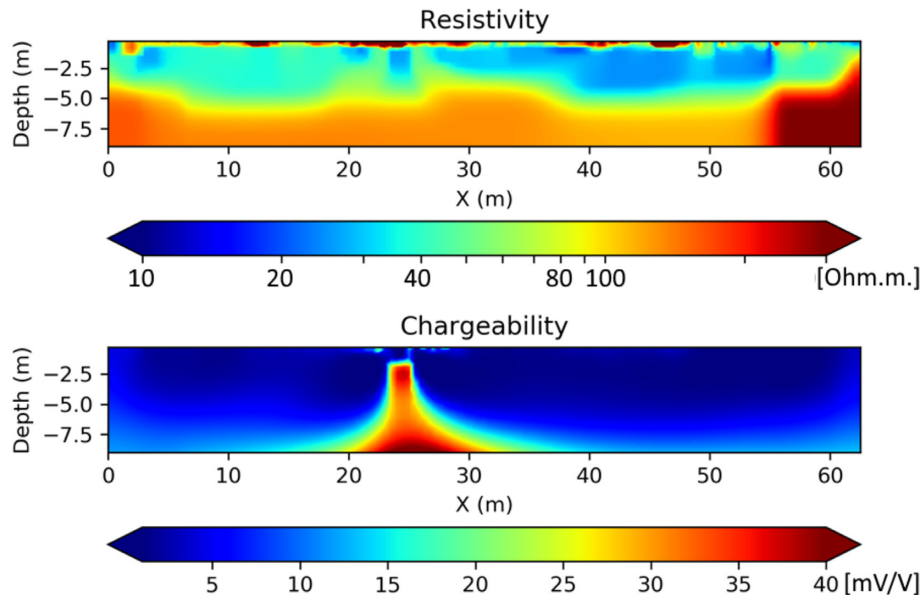

Figure 13. Inverted model of resistivity (top) and chargeability (bottom) of the baseline for Line3.

at about 25 m along the profile. This anomaly is of an order of magnitude higher than the background levels, thereby masking the subtle changes in the background.

Line 4 (Fig. 14) shows a smoother and more homogeneous pattern in the time-lapse inversions. Nevertheless, a different distribution of the changes in resistivity is identified in the portion of the profile about from 7 to 37 m (western portion) with a general decrease in resistivity.

Fig. 16 compares the resistivity of the shallower soil of Line 3 and Line 4 with soil temperature. The time-series of Line 3 and Line 4 are obtained by averaging the inverted resistivity for each available time step in a depth slice of 1.5 from the topographic surface. The soil temperature data are collected via a temperature probe (107 Thermistor probe, Campbell Scientific) buried at 20 cm depth in the central part of Line3 (27 m along the profile), which samples every 10 min. The rapid increase of resistivity in March

2018 and February 2019 (Fig. 16), which can be directly correlated with the observations in the raw-data (Fig. 2), is evidently caused by frozen ground when the soil temperature drops below 0 °C.

Figs 18 and 17 summarize the changes in resistivity (left plot) and chargeability (right plot) over the monitoring period, for Lines 4 and 3, respectively. The geophysical parameters (percentage change in resistivity and absolute change in chargeability) are obtained from the inverted results presented in Figs 14 and 15. The electrical quantities are averaged over three areas of higher interest that present different patterns during time. The western area along Line 3 (marked as 'a' in Fig. 17) coincides with the portion of ground that was treated by injecting a fluid containing a bacteria consortium and nutrients. The central area of Line 3 ('b' in Fig. 17) was treated by injecting a solution of zerovalent iron and bacteria. The eastern area of Line 3 ('c' in Fig. 17) represents the untreated and
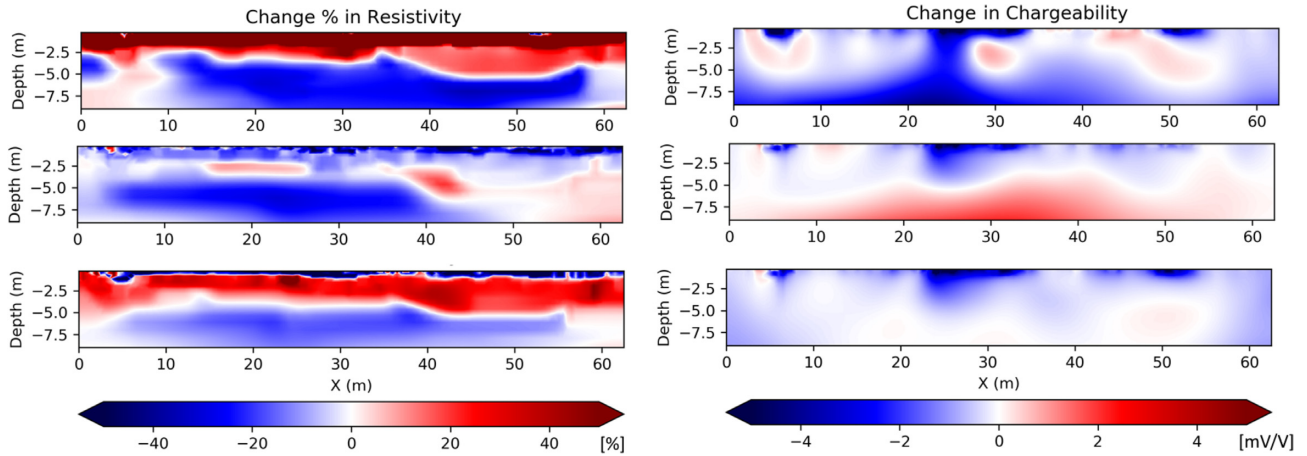
Figure 14. Examples of time-lapse inversions of Line4: from dates 2018 March 8 (top row), 2018 October 21 (middle row) and 2019 February 27 (bottom row). Percentage change in resistivity (left-hand column) and absolute change in chargeability (right-hand column) compared to baseline data set.

Figure 15. Examples of time-lapse inversions of Line3: from dates 2018 March 8 (top row), 2018 October 21 (middle row) and 2019 February 27 (bottom row). Percentage change in resistivity (left-hand column) and absolute change in chargeability (right-hand column) compared to baseline data set.
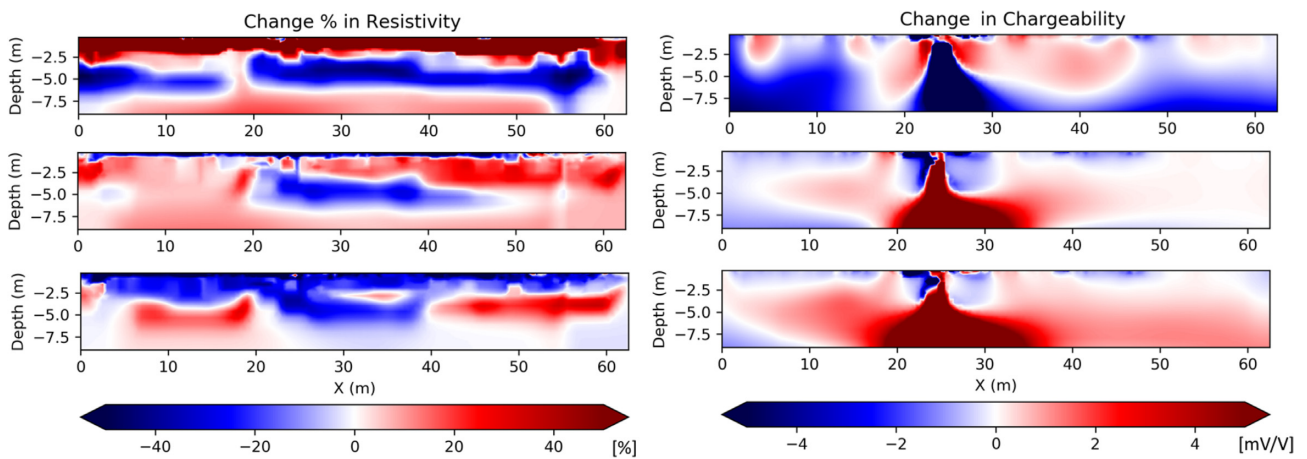
uncontaminated ground. Three areas with the same relative location along the profile are selected for Line 4 (Fig. 18).

Area *c* represents a volume of untreated and uncontaminated ground, both for Line 3 and Line 4 (Figs 17 and 18 respectively). It is evident that the pattern of resistivity changes in those areas shows a high similarity, both in the shape of the curve over time and in the values of resistivity changes. The absolute changes in chargeability display the same behaviour, even if the values are confined in a narrow range (between -1 and 1 mV V^{-1}). These deviations from the baseline can be linked to seasonal variations. In particular, temperature and fluid salinity might play a dominant role, as both resistivity and chargeability increase during summer and decrease in winter.

Areas *a* and area *b* along Line 3 (Fig. 17) show completely different patterns over time. Central area *b* is represented by a consistent decrease in resistivity, while western area *a* has a pattern that reflects the untreated and uncontaminated ground (area *c*). The evident drop in resistivity of area *b* can be explained by the nature of the injected remediation product that is a solution containing coated particles of zerovalent iron. When the coating is dissolved, the iron particles start to oxidize and reduce the bulk resistance of the ground. The drop in the resistivity values is not associated with similar fluctuations in the chargeability values, even if they are not straightforward to interpret, since an anomaly connected to some buried

infrastructure strongly influences this area. The fact that area *a*, treated with a bioremediation product, has a similar pattern as the uncontaminated and untreated area *c* could mean that the injection of the bacteria consortium was not successful, or that the injected media has no impact in the geoelectrical signal.

Fig. 19 shows part of the results from an extensive geochemical survey that was performed to monitor and validate the *in situ* pilot bioremediation (Åkesson *et al.* 2021). The analyses were performed on water samples collected from wells with filters in the sand media, which are located between the crystalline bedrock and the clay layer. The data are sampled in boreholes that are closely located to Line 3 and 4 (Fig. 8). The concentration of PCE is dramatically decreased after the bioremediation was initiated and the concentration of the degradation products, specifically cis-DCE, is increased, for both area *a* (corresponding to samples in LU4) and area *b* (corresponding to samples in LU6). Based on the geochemical data, it seems that degradation is occurring in both area *a* and area *b*, hence the difference in the geophysical response is mainly due to the bioremediation agents.

The time-series of inverted geophysical parameters along Line 4 in area *a* and area *b* (Fig. 18) do not show the same pattern as along Line 3 (Fig. 17). Area *a'* and area *b'* are characterized by an almost identical curve, both for resistivity and chargeability changes. They differ from the uncontaminated area *c'* and they
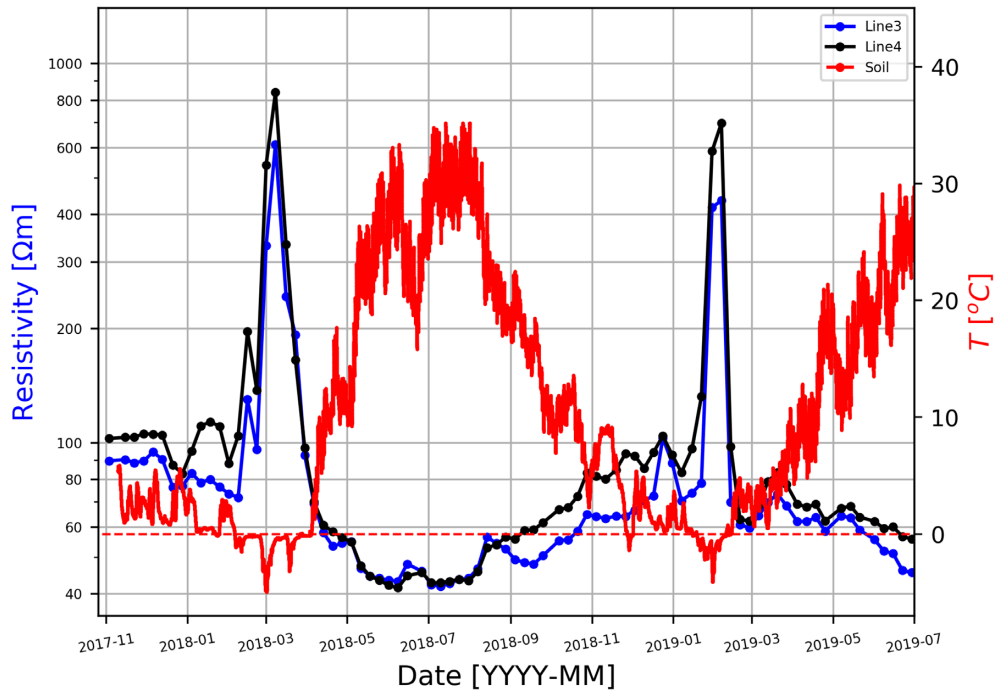
Figure 16. Averaged inverted resistivity values of the shallower soil (X m deep) for Line 3 (blue line) and Line 4 (black line) over the monitoring period. The red solid line represents the soil temperature, measured at the depth of 20 cm, while the red dashed line highlights the level of 0 °C.
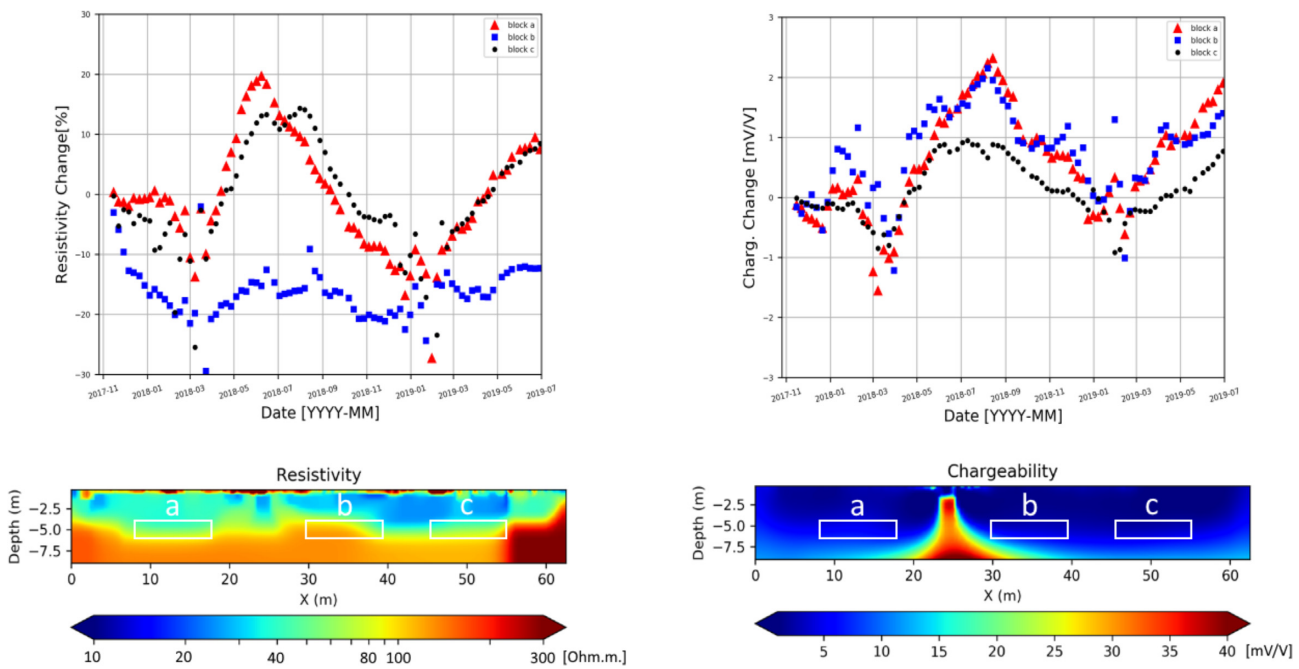

Figure 17. Analysis of the time-dependent variations of resistivity (left) and chargeability (right) for Line 3. Resistivity is represented as percentage changes of inverted data respect to background, while chargeability is the absolute variation of inverted integral chargeability respect to background values. The values of the plots are calculated averaging inside the three areas (a–c) highlighted in the inverted results from the baseline (bottom).

present an overall reduction in resistivity. The curves resemble a blended pattern of area *a* and area *b* of Line 3 (Fig. 17). This fact suggests a possible explanation for these different anomalies. Line 4 is not orthogonal to the groundwater flow (showed in Fig. 8), so the fluids that intersect the geophysical profile could be a mixture of both remediation products that are well separated along Line 3, due to its proximity to the treated ground. It is clearly indicating that

the geophysical response from the degradation of zerovalent iron particles is dominant, even if the degradation products are probably diluted as is suggested by relatively higher values of resistivity in area *b'* compared to area *b* (Line 3, Fig. 17).

This pattern can be recognised also in Fig. 19, where the iron concentration is generally increased for area *b* (LU6) due to the injection of the remediation agent, while it is not the case for area
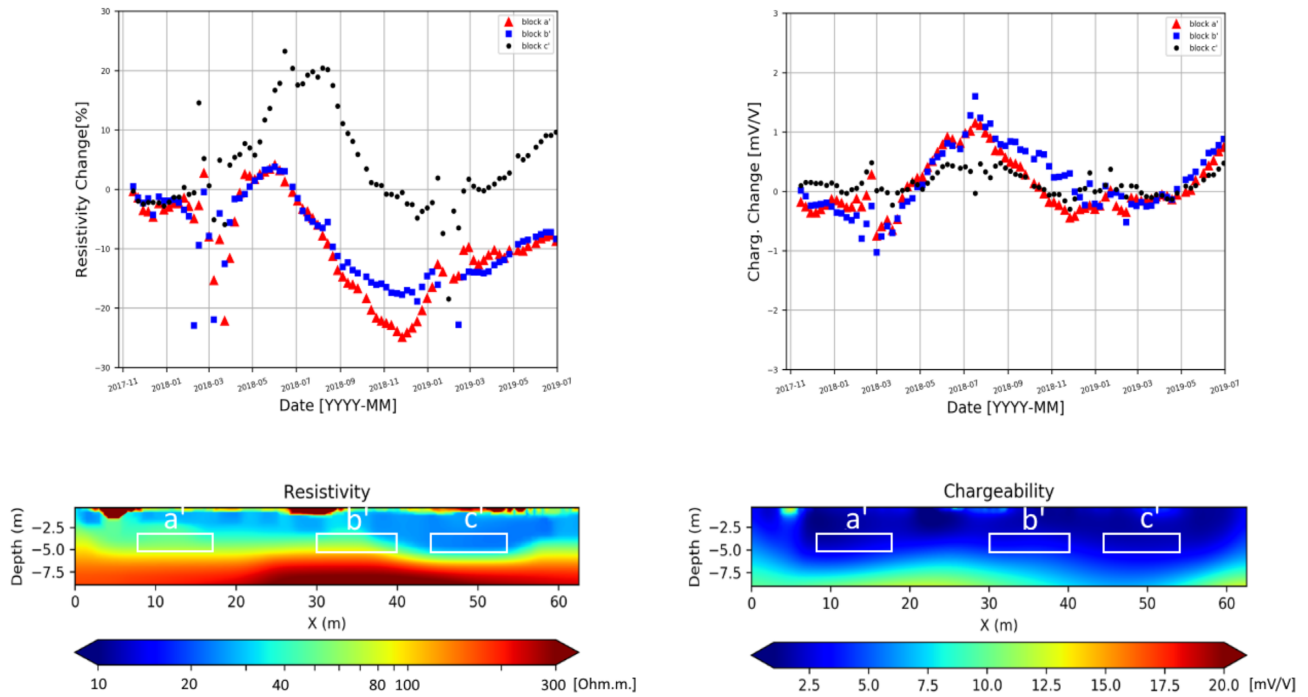
Figure 18. Analysis of the time-dependent variations of resistivity (left) and chargeability (right) for Line 4. Resistivity is represented as percentage changes of inverted data respect to background, while chargeability is the absolute variation of inverted integral chargeability respect to background values. The values of the plots are calculated averaging inside the three areas (a–c) highlighted in the inverted results from the baseline (bottom).
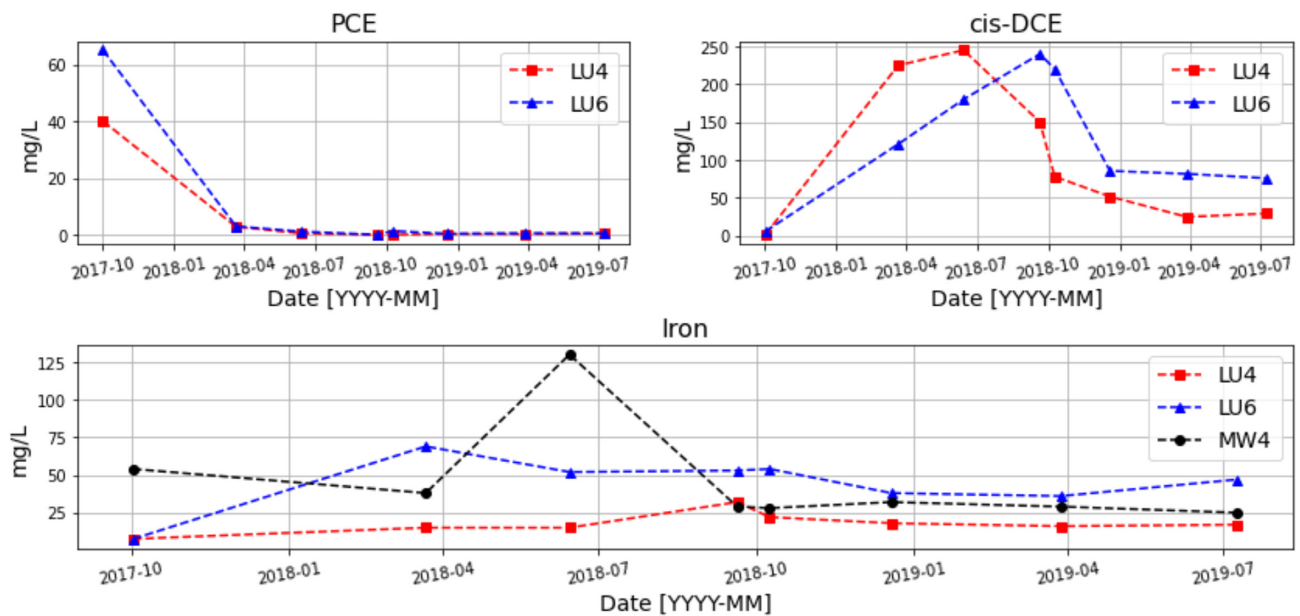

Figure 19. Geochemical results that show the PCE (top left), cis-DCE (top right) and iron (bottom) concentrations in the water samples (see Fig. 8 for boreholes location). Water samples were collected by Sofia Åkesson and the WSP on behalf of the Swedish Geological Survey (SGU) as part of the survey for monitoring the effects of *in situ* bioremediation.

a (LU4). The injected agent, containing iron particles, has then migrated downgradient and can be seen in MW4 as a spike in iron concentration after approximately 6–8 months. MW4 is located NW of line 4 (Fig. 8) and the increase in the iron concentration is in good correlation with the resistivity trend of block *a'* (Fig. 18). The drop in resistivity of block *a* and *b* occurs around the same time.

The shape of the curves that display the variations of inverted resistivity and chargeability are consistent over the entire period of 20 months. This strengthens the claim that the applied methodology for processing and inverting the geophysical data is robust and has great potential in long-term monitoring systems, especially for enhancing the interpretation of long-term geochemical processes. The results can successfully capture the changes due to the injection

of the remediation agents, however they need to be further optimized (and possible temperature corrected) in order to capture the much smaller changes due to the degradation of the contaminants. Therefore, the proposed scheme can be applied in case of available long-term monitoring to reveal periods of interest for which a more detailed analysis needs to be carried out.

CONCLUSIONS

This work describes the different components needed for a long-term geophysical monitoring using the DCIP method with high temporal frequency sampling. The proposed routines for data processing and inversion are first tested against a simulated time-lapse experiment and are then applied on field data, collected on a site contaminated by chlorinated solvents, where a pilot *in situ* remediation is on-going since November 2017.

The results from the simulated time-lapse experiment show that the proposed workflow is very effective in removing spikes and outliers. The inversion results can resolve the simulated changes in the different areas. The results from the field data show strong seasonal variations due to frozen ground and marked yearly variations due to changes in the air temperature. Furthermore, the areas where two different remediation agents were injected appear to have different behaviours in the inverted time-series models. The proposed scheme can resolve the changes due to the remediation agents since they are more dominant but is not successful in resolving changes that can be linked to the biochemical processes. Furthermore, the daily measurements allow to capture smoother seasonal variations, which can be in the range of 25 per cent change in resistivity and 4 mV V^{-1} change in chargeability. These seasonal changes might be falsely interpreted as natural changes if the measurements are repeated at widely spaced time intervals.

It is evident that the shapes of the inverted resistivity and chargeability time-series curves, extracted from different areas of the profile, are consistent over the entire period of 20 months. This shows that the methodology used is very robust when applied to the experimental data set from the Alingsås site. This outcome together with the analysis of the synthetic data set suggests a strong potential for long-term monitoring in other sites. The different components of the system are automated separately and can be integrated together with some further optimization. It possible to automatically acquire daily data that will be pipelined through the processing algorithms, the inversion routines and the visualization scripts, making real-time DCIP monitoring possible. The inverted results would be visualized, with a short delay due to data transferring and processing, and the system can be horizontally scaled to be applied in multiple sites.

ACKNOWLEDGEMENTS

DATA AVAILABILITY

The data sets generated and/or analysed during the current study are available from the corresponding author on reasonable request. The authors declare no potential conflicts of interest with respect to the research, authorship, and/or publication of this article.

REFERENCES

Abdulsamad, F., Revil, A., Soueid Ahmed, A., Coperey, A., Karaoulis, M., Nicaise, S. & Peyras, L., 2019. Induced polarization tomography applied to the detection and the monitoring of leaks in embankments, *Eng. Geol.,* **254,** 89–101.

Åkesson, S., Sparrenbom, C.J., Holmstrand, H. & Paul, C.J., 2021. Biogeochemical changes during in situ remediation actions of tetrachloroethene, unpublished manuscript.

Apgar, M.A. & Langmuir, D., 1971. Ground-water pollution potential of a landfill above the water table, *Groundwater,* **9,** 76–96.

Arosio, D., Munda, S., Tresoldi, G., Papini, M., Longoni, L. & Zanzi, L., 2017. A customized resistivity system for monitoring saturation and seepage in earthen levees: installation and validation, *Open Geosci.,* **9,** 457–467.

Atekwana, E.A. & Atekwana, E.A., 2010. Geophysical signatures of microbial activity at hydrocarbon contaminated sites: a review, *Surv. Geophys.,* **31,** 247–283.

Atekwana, E.A., Atekwana, E., Legall, F.D. & Krishnamurthy, R.V., 2005. Biodegradation and mineral weathering controls on bulk electrical conductivity in a shallow hydrocarbon contaminated aquifer, *J. Contam. Hydrol.,* **80,** 149–167.

Auken, E., Doetsch, J., Fiandaca, G., Christiansen, A.V., Gazoty, A., Cahill, A.G. & Jakobsen, R., 2014. Imaging subsurface migration of dissolved CO$_2$ in a shallow aquifer using 3-D time-lapse electrical resistivity tomography, *J. Appl. Geophys.,* **101,** 31–41.

Bernstone, C., Dahlin, T., Ohlsson, T. & Hogland, W., 2000. DC-resistivity mapping of internal landfill structures: two pre-excavation surveys, *Environ. Geol.,* **39,** 360–371.

Brunet, P., Clément, R. & Bouvier, C., 2010. Monitoring soil water content and deficit using Electrical Resistivity Tomography (ERT)—a case study in the Cevennes area, France, *J. Hydrol.,* **380,** 146–153.

Cabral, A., Demers, L. & Ciubotariu, R., 2000. Potential contaminant migration at a contaminated soils landfill site in Quebec, *Presented at the Geotechnical Special Publication,* pp. 68–80.

Cassiani, G., Kemna, A., Villa, A. & Zimmermann, E., 2009. Spectral induced polarization for the characterization of free-phase hydrocarbon contamination of sediments with low clay content, *Near Surf. Geophys.,* **7,** 547–562.

Caterina, D., Flores Orozco, A. & Nguyen, F., 2017. Long-term ERT monitoring of biogeochemical changes of an aged hydrocarbon contamination, *J. Contam. Hydrol.,* **201,** 19–29.

Chambers, J.E., Kuras, O., Meldrum, P.I., Ogilvy, R.D. & Hollands, J., 2006. Electrical resistivity tomography applied to geologic, hydrogeologic, and engineering investigations at a former waste-disposal site, *Geophysics,* **71,** B231–B239.

Chambers, J.E., Meldrum, P.I., Gunn, D.A., Wilkinson, P.B., Kuras, O., Weller, A.L. & Ogilvy, R.D., 2009. Hydrogeophysical monitoring of landslide processes using automated time-lapse electrical resistivity tomography (ALERT), *Presented at the Near Surface 2009—15th European Meeting of Environmental and Engineering Geophysics,* https://doi.org/10.3997/2214-4609.20147066.

Chirindja, F.J., Dahlin, T. & Juizo, D., 2017. Improving the groundwater-well siting approach in consolidated rock in Nampula Province, Mozambique, *Hydrogeol. J.,* **25,** 1423–1435.

Dahlin, T. & Leroux, V., 2012. Improvement in time-domain induced polarization data quality with multi-electrode systems by separating current and potential cables, *Near Surf. Geophys.,* **10,** 545–565.

Dahlin, T. & Zhou, B., 2006. Multiple-gradient array measurements for multichannel 2D resistivity imaging, *Near Surf. Geophys.,* **4,** 113–123.

Dahlin, T., Leroux, V. & Nissen, J., 2002. Measuring techniques in induced polarisation imaging, *J. Appl. Geophys.,* **50,** 279–298.

Danielsen, B.E. & Dahlin, T., 2009. Comparison of geoelectrical imaging and tunnel documentation at the Hallandsås Tunnel, Sweden, *Eng. Geol.,* **107,** 118–129.

Danielsen, B.E. & Dahlin, T., 2012. The applicability of geoelectrical methods in pre-investigation for construction in rock, *Presented at the ISRM International Symposium—EUROCK 2012.*

Davis, C.A. & Atekwana, E., 2006. Potential application of biogeophysics to EOR and remediation investigations, in *SEG Technical Program Expanded Abstracts,* Vol. 25, pp. 1471–1474.

Davis, C.A., Atekwana, E., Atekwana, E., Slater, L.D., Rossbach, S. & Mormile, M.R., 2006. Microbial growth and biofilm formation in geologic media is detected with complex conductivity measurements, *Geophys. Res. Lett.,* **33,** https://doi.org/10.1029/2006GL027312.

Fernandez, P.M., Bloem, E., Binley, A., Philippe, R.S.B.A. & French, H.K., 2019. Monitoring redox sensitive conditions at the groundwater interface using electrical resistivity and self-potential, *J. Contam. Hydrol.,* **226,** 103517.

Fetter, C.W., 2001. *Applied Hydrogeology,* 4th edn, Prentice Hall.

Flores Orozco, A., Kemna, A., Oberdörster, C., Zschornack, L., Leven, C., Dietrich, P. & Weiss, H., 2012a. Delineation of subsurface hydrocarbon contamination at a former hydrogenation plant using spectral induced polarization imaging, *J. Contam. Hydrol.,* **136-137,** 131–144.

Flores Orozco, A., Kemna, A. & Zimmermann, E., 2012b. Data error quantification in spectral induced polarization imaging, *Geophysics,* **77,** E227–E237.

Flores Orozco, A., Williams, K.H. & Kemna, A., 2013. Time-lapse spectral induced polarization imaging of stimulated uranium bioremediation, *Near Surf. Geophys.,* **11,** 531–544.

Flores Orozco, A. *et al.,* 2015. Monitoring the injection of microscale zerovalent iron particles for groundwater remediation by means of complex electrical conductivity imaging, *Environ. Sci. Technol.,* **49,** 5593–5600.

Flores Orozco, A., Kemna, A., Binley, A. & Cassiani, G., 2019. Analysis of time-lapse data error in complex conductivity imaging to alleviate anthropogenic noise for site characterization, *Geophysics,* **84,** B181–B193.

Forquet, N. & French, H.K., 2012. Application of 2D surface ERT to on-site wastewater treatment survey, *J. Appl. Geophys.,* **80,** 144–150.

Fortier, R., LeBlanc, A.-M., Allard, M., Buteau, S. & Calmels, F., 2008. Internal structure and conditions of permafrost mounds at Umiujaq in Nunawik, Canada, inferred from field investigation and electrical resistivity tomography, *Can. J. Earth Sci.,* **45,** 367–387.

Gamal, H., Bageri, B.S., Elkatatny, S. & Patil, S., 2021. Investigating the alteration of sandstone pore system and rock features by role of weighting materials, *ACS Omega,* **6,** 4100–4110.

Garrido, T., Fraile, J., Niñerola, J.M., Figueras, M., Ginebreda, A. & Olivella, L., 2000. Survey of ground water pesticide pollution in rural areas of Catalonia (Spain), *Int. J. Environ. Anal. Chem.,* **78,** 51–65.

Gazoty, A., Fiandaca, G., Pedersen, J., Auken, E. & Christiansen, A.V., 2012. Mapping of landfills using time-domain spectral induced polarization data: the Eskelund case study, *Near Surf. Geophys.,* **10,** 575–586.

Heenan, J. *et al.,* 2015. Electrical resistivity imaging for long-term autonomous monitoring of hydrocarbon degradation: lessons from the deepwater horizon oil spill, *Geophysics,* **80,** B1–B11.

Hopkins, G.J. & Popalisky, J.R., 1970. Influence of an industrial waste landfill operation on a public water supply, *J. Water Pollut. Control Fed.,* **42,** 431–436.

Johansson, S., Sparrenbom, C., Fiandaca, G., Lindskog, A., Olsson, P.-I., Dahlin, T. & Rosqvist, H., 2017. Investigations of a Cretaceous limestone with spectral induced polarization and scanning electron microscopy, *Geophys. J. Int.,* **208,** 954–972.

Kelly, W.E., 1966. Ground-water pollutions near a landfill, *ASCE J. Environ. Eng.,* **102,** 1189–1199.

Kolpin, D.W., Barbash, J.E. & Gilliom, R.J., 2000. Pesticides in ground water of the United States, 1992–1996, *Ground Water,* **38,** 858–863.

Kuras, O. *et al.,* 2016. Geoelectrical monitoring of simulated subsurface leakage to support high-hazard nuclear decommissioning at the Sellafield Site, UK, *Sci. Total Environ.,* **566-567,** 350–359.

Leroux, V. & Dahlin, T., 2006. Time-lapse resistivity investigations for imaging saltwater transport in glaciofluvial deposits, *Environ. Geol.,* **49,** 347–358.

Liapis, K.S., Miliadis, G.E. & Tsiropoulos, N.G., 2000. Confirmation of pesticides in water samples by mass spectrometry, *Bull. Environ. Contam. Toxicol.,* **65,** 811–817.

Loke, M.H., Chambers, J.E., Rucker, D.F., Kuras, O. & Wilkinson, P.B., 2013. Recent developments in the direct-current geoelectrical imaging method, *J. Appl. Geophys.,* **95,** 135–156.

Mainoo, P.A., Manu, E., Yidana, S.M., Agyekum, W.A., Stigter, T., Duah, A.A. & Preko, K., 2019. Application of 2D-Electrical resistivity tomography in delineating groundwater potential zones: case study from the voltaian super group of Ghana, *J. Afr. Earth Sci.,* **160,** 103618.

Maurya, P.K. *et al.,* 2018a. Subsurface imaging of water electrical conductivity, hydraulic permeability and lithology at contaminated sites by induced polarization, *Geophys. J. Int.,* **213,** 770–785.

Maurya, P.K., Fiandaca, G., Christiansen, A.V. & Auken, E., 2018b. Field-scale comparison of frequency- and time-domain spectral induced polarization, *Geophys. J. Int.,* **214,** 1441–1465.

Mgbolu, C.C., Obiadi, I.I., Obiadi, C.M., Okolo, C.M. & Irumhe, P.E., 2019. Integrated groundwater potentials studies, aquifer hydraulic characterisation and vulnerability investigations of parts of Ndokwa, Niger Delta Basin, Nigeria, *Solid Earth Sci.,* **4,** 102–112.

Mishra, U., Chandroth, A., Basantaray, A.K., Chel, S. & Mandal, A., 2019. Assessing chromite ore processing residue (COPR) waste dump using electrical resistivity tomography (ERT): a case study from Umaran, Kanpur, India, *Environ. Monit. Assess.,* **191,** https://doi.org/10.1007/s10661-019-7646-2.

Nivorlis, A., Dahlin, T., Rossi, M., Höglund, N. & Sparrenbom, C., 2019. Multidisciplinary characterization of chlorinated solvents contamination and in-situ remediation with the use of the direct current resistivity and time-domain induced polarization tomography, *Geosciences,* **9,** https://doi.org/10.3390/geosciences9120487.

Ntarlagiannis, D., Robinson, J., Soupios, P. & Slater, L., 2016. Field-scale electrical geophysics over an olive oil mill waste deposition site: evaluating the information content of resistivity versus induced polarization (IP) images for delineating the spatial extent of organic contamination, *J. Appl. Geophys.,* **135,** 418–426.

Olsson, P.-I., Dahlin, T., Fiandaca, G. & Auken, E., 2015. Measuring time-domain spectral induced polarization in the on-time: decreasing acquisition time and increasing signal-to-noise ratio, *J. Appl. Geophys.,* **123,** 316–321.

Olsson, P.-I., Fiandaca, G., Larsen, J.J., Dahlin, T. & Auken, E., 2016. Doubling the spectrum of time-domain induced polarization by harmonic de-noising, drift correction, spike removal, tapered gating and data uncertainty estimation, *Geophys. J. Int.,* **207,** 774–784.

Olsson, P.-I., Fiandaca, G., Maurya, P.K., Dahlin, T. & Auken, E., 2019. Effect of current pulse duration in recovering quantitative induced polarization models from time-domain full-response and integral chargeability data, *Geophys. J. Int.,* **218,** 1739–1747.

Ottosen, C.B. *et al.,* 2021. Assessment of chlorinated ethenes degradation after field scale injection of activated carbon and bioamendments: application of isotopic and microbial analyses, *J. Contam. Hydrol.,* **240,** 103794.

Park, S., Yi, M.-J., Kim, J.-H. & Shin, S.W., 2016. Electrical resistivity imaging (ERI) monitoring for groundwater contamination in an uncontrolled landfill, South Korea, *J. Appl. Geophys.,* **135,** 1–7.

Power, C., Gerhard, J.I., Karaoulis, M., Tsourlos, P. & Giannopoulos, A., 2014. Evaluating four-dimensional time-lapse electrical resistivity tomography for monitoring DNAPL source zone remediation, *J. Contam. Hydrol.,* **162-163,** 27–46.

Power, C., Tsourlos, P., Ramasamy, M., Nivorlis, A. & Mkandawire, M., 2018. Combined DC resistivity and induced polarization (DC-IP) for mapping the internal composition of a mine waste rock pile in Nova Scotia, Canada, *J. Appl. Geophys.,* **150,** 40–51.

Rai, N., Sjöberg, V., Forsberg, G., Karlsson, S., Olsson, P.-E. & Jass, J., 2019. Metal contaminated soil leachates from an art glass factory elicit stress response, alter fatty acid metabolism and reduce lifespan in Caenorhabditis elegans, *Sci. Total Environ.,* **651,** 2218–2227.

Röling, W.F.M., Van Breukelen, B.M., Braster, M., Goeltom, M.T., Groen, J. & Van Verseveld, H.W., 2000. Analysis of microbial communities in a landfill leachate polluted aquifer using a new method for anaerobic physiological profiling and 16S rDNA based fingerprinting, *Microb. Ecol.,* **40,** 177–188.

Ronczka, M., Wisén, R. & Dahlin, T., 2018. Geophysical pre-investigation for a Stockholm tunnel project: joint inversion and interpretation of geoelectric and seismic refraction data in an urban environment, *Near Surf. Geophys.,* **16,** 258–268.

Rossi, M., Dahlin, T., Olsson, P.-I. & Günther, T., 2018. Data acquisition, processing and filtering for reliable 3D resistivity and time-domain induced polarisation tomography in an urban area: field example of Vinsta, Stockholm, *Near Surf. Geophy.,* **16,** 220–229.

Rücker, C., Günther, T. & Wagner, F.M., 2017. pyGIMLi: an open-source library for modelling and inversion in geophysics, *Comput. Geosci.,* **109,** 106–123.

Saneiyan, S., Ntarlagiannis, D., Ohan, J., Lee, J., Colwell, F. & Burns, S., 2019. Induced polarization as a monitoring tool for in-situ microbial induced carbonate precipitation (MICP) processes, *Ecol. Eng.,* **127,** 36–47.

Sedlazeck, K.P., Vollprecht, D., Müller, P., Mischitz, R. & Gieré, R., 2020. Impact of an in-situ Cr(VI)-contaminated site remediation on the groundwater, *Environ. Sci. Pollut. Res.,* **27,** 14 465–14 475.

SEPA, 2014. Nationell Plan för Fördelning av Statliga Bidrag för Efterbehandling, Report 6617. Swedish Environmental Protection Agency: Stockholm, Sweden Volume 30.

Sjödahl, P., Dahlin, T., Johansson, S. & Loke, M.H., 2008. Resistivity monitoring for leakage and internal erosion detection at Hällby embankment dam, *J. Appl. Geophys.,* **65,** 155–164.

Sjödahl, P., Dahlin, T. & Johansson, S., 2009. Embankment dam seepage evaluation from resistivity monitoring data, *Near Surf. Geophys.,* **7,** 463–474.

Sparrenbom, C.J., Åkesson, S., Johansson, S., Hagerberg, D. & Dahlin, T., 2017. Investigation of chlorinated solvent pollution with resistivity and induced polarization, *Sci. Total Environ.,* **575,** 767–778.

Telford, W.M., Geldart, L.P. & Sheriff, R.E., 1991. *Applied Geophysics,* 2nd edn, Cambridge Univ. Press.

Ustra, A.T., Elis, V.R., Mondelli, G., Zuquette, L.V. & Giacheti, H.L., 2012. Case study: a 3D resistivity and induced polarization imaging from downstream a waste disposal site in Brazil, *Environ. Earth Sci.,* **66,** 763–772.

Virtanen, P. *et al.*, 2020. SciPy 1.0: fundamental algorithms for scientific computing in Python, *Nat. Methods,* **17,** 261–272.

Vitali, M. *et al.*, 2021. Environmental status of an Italian site highly polluted by illegal dumping of industrial wastes: the situation 15 years after the judicial intervention, *Sci. Total Environ.,* **762,** 144100.

Wang, T.-P., Chen, Y.-T., Chen, C.-C., Tung, T.-H., Cheng, S.-N. & Yu, C.-Y., 2020. Application of cross-hole electrical resistivity tomography to groundwater contaminated remediation site, *Terr. Atmos. Ocean. Sci.,* **31,** 1–15.

Weller, A. & Slater, L., 2019. Permeability estimation from induced polarization: an evaluation of geophysical length scales using an effective hydraulic radius concept, *Near Surf. Geophys.,* **17,** 581–594.

Zago, M.M., Fries, M. & Ramires, J.E.F., 2020. Groundwater infiltration in a gold mine–a geoelectrical investigation model as an aid to dewatering process determination, *J. Appl. Geophys.,* **172,** 103909.

Zhou, Y., Liu, X. & Wang, J., 2019. Characterization of microplastics and the association of heavy metals with microplastics in suburban soil of central China, *Sci. Total Environ.,* **694,** 133798.